A study of pressure-driven displacement flow of two immiscible liquids using a multiphase lattice Boltzmann approach

Prasanna R. Redapangu, Kirti Chandra Sahu, and S. P. Vanka

Citation: Physics of Fluids (1994-present) **24**, 102110 (2012); doi: 10.1063/1.4760257
View online: http://dx.doi.org/10.1063/1.4760257
View Table of Contents: http://scitation.aip.org/content/aip/journal/pof2/24/10?ver=pdfcov
Published by the AIP Publishing

A study of pressure-driven displacement flow of two immiscible liquids using a multiphase lattice Boltzmann approach

Prasanna R. Redapangu,[1] Kirti Chandra Sahu,[1,a)] and S. P. Vanka[2]
[1]*Department of Chemical Engineering, Indian Institute of Technology, Hyderabad, Yeddumailaram 502 205, Andhra Pradesh, India*
[2]*Department of Mechanical Science and Engineering, University of Illinois at Urbana-Champaign, Urbana, Illinois 61801, USA*

(Received 7 January 2012; accepted 3 October 2012; published online 19 October 2012)

The pressure-driven displacement of two immiscible fluids in an inclined channel in the presence of viscosity and density gradients is investigated using a multiphase lattice Boltzmann approach. The effects of viscosity ratio, Atwood number, Froude number, capillary number, and channel inclination are investigated through flow structures, front velocities, and fluid displacement rates. Our results indicate that increasing viscosity ratio between the fluids decreases the displacement rate. We observe that increasing the viscosity ratio has a non-monotonic effect on the velocity of the leading front; however, the velocity of the trailing edge decreases with increasing the viscosity ratio. The displacement rate of the thin-layers formed at the later times of the displacement process increases with increasing the angle of inclination because of the increase in the intensity of the interfacial instabilities. Our results also predict the front velocity of the lock-exchange flow of two immiscible fluids in the exchange flow dominated regime. A linear stability analysis has also been conducted in a three-layer system, and the results are consistent with those obtained by our lattice Boltzmann simulations. © *2012 American Institute of Physics*. [http://dx.doi.org/10.1063/1.4760257]

I. INTRODUCTION

The pressure-driven displacement flow of one fluid by another fluid is common in many industrial processes, such as transportation of crude oil in pipelines,[1] oil recovery, food-processing, coating, etc. The cleaning of plants also involves the removal of viscous fluids by fast-flowing water streams.[2] In enhanced oil recovery, hydrocarbon solvent or supercritical carbon dioxide is used to displace oil from an oil reservoir.

When a less viscous fluid displaces a more viscous one, a two-layer/core-annular flow is obtained in most part of the channel/pipe as the elongated "finger" of the less viscous fluid penetrates into the bulk of the more viscous one.[3] The interface between the two fluids becomes unstable forming Yih-type instability for immiscible[4] and Kelvin-Helmholtz (KH) type instabilities and "roll-up" structures for miscible flows. A review of the phenomenon occurring in porous media (commonly known as viscous fingering) can be found in Ref. 5. In pressure-driven two-layer/core-annular flows, several authors have conducted linear stability analyses by considering the fluids to be immiscible[4,6–8] and miscible.[3,9–12] This problem was also studied by many researchers experimentally[13,14] and numerically.[15–18] In miscible core-annular flows, the thickness of the more viscous fluid layer left on the pipe walls and the speed of the propagating "finger" were experimentally investigated by many authors[19–23] and the axisymmetric and "corkscrew" patterns were found.[24–28] In neutrally-buoyant core-annular pipe flows, d'Olce *et al.*[29] observed axisymmetric "pearl" and "mushroom"

a)ksahu@iith.ac.in.

patterns at high Schmidt number. By an asymptotic analysis, Yang and Yortsos[30] studied miscible displacement Stokes flow between parallel plates and in cylindrical capillary tube with large aspect ratio. They found viscous fingering instability for large viscosity ratio and the displacement efficiency decreases with increasing viscosity ratio. Goyal and Meiburg[31] studied miscible displacement flows in a vertical Hele-Shaw cell with less-viscous fluid displacing a more-viscous one. They found that the flow develops as a result of linear instability, and the front velocity increases with increasing unstable density stratification and decreasing diffusion. The flow fields obtained by their simulations are qualitatively similar to those observed in the experiment of Petitjeans and Maxworthy[21] in a capillary tube and in the theoretical predictions of Lajeunesse *et al.*[25] in Hele-Shaw cells.

Sahu *et al.*[32] studied pressure-driven miscible displacement flow in an inclined channel via numerical solution of the Navier-Stokes equations coupled to a convective-diffusion equation for the concentration of the more viscous fluid. The viscosity and density are assumed to be a function of the concentration of the more viscous fluid and the effects of density ratio, Froude number, and channel inclination were investigated. Their results demonstrated that the rate of mixing and displacement of the more viscous fluid are promoted by the development of KH-type instabilities, and enhanced with increasing density ratio and Froude number. The mixing rates were also shown to increase with increasing inclination angles when the displaced fluid is also the denser one. Recently, Taghavi *et al.*[33,34] studied the effects of imposed mean flow on a buoyant exchange flow of two miscible fluids in a near horizontal pipe/channel. For very low imposed velocity, they observed an inertial gravity current and KH-like instabilities in the interfacial region separating the fluids. The flow becomes stable for higher imposed flow with the absence of KH instabilities and consequent decreased mixing. This behavior is counterintuitive since more energy is injected into the system as the imposed flow is increased. Non-Newtonian effects on miscible displacement flows in vertical narrow eccentric annuli were experimentally studied by Mohammadi *et al.*[35] They demonstrated that suitable choices of viscosity ratio, density ratio, and flow rate result in steady displacement flows. In the case of steady flow, they observed that eccentricity drives a strong azimuthal counter-current flow above/below the interface resulting in an advancing spike.

Most numerical studies of displacement flows solved the continuum Navier-Stokes equations using a finite volume/element/spectral method. The lattice Boltzmann method (LBM) is an alternative to solve the Navier-Stokes equations for the study of fluid flows. This is a mesoscopic model that has its origins in the kinetic theory. The LBM solves discrete density distribution functions and obtains the velocities and density as moments of this distribution function. In comparison with a solution of the Navier-Stokes equations, LBM is a simple, efficient, and easily parallelizable technique. It involves only three basic steps: (a) collision, (b) streaming, and (c) calculation of the flow variables. It can include mesoscopic flow physics such as velocity slip, surface tension force, and other inter-molecular forces. There are four distinctly different LBM approaches for multiphase flows, namely, the color segregation method of Gunstensen *et al.*,[36] method of Shan and Chen,[37,38] free energy approach of Swift *et al.*,[39] method of He *et al.*[40] A review of the work on the first three approaches was provided by Chen *et al.*[41] Using the multiphase LBM approach proposed by He and co-workers,[40,42] recently, Sahu and Vanka[43] studied the buoyancy-driven interpenetration of two immiscible fluids in an inclined channel (commonly known as "lock-exchange" problem). The effects of tilt angle, Atwood number, Reynolds number, and surface tension were investigated in terms of flow structures and front velocity. Rakotomalala *et al.*[44] also studied the miscible displacement flow between two parallel plates using the Bhatnagar-Gross-Krook (BGK) lattice gas method.

As the above brief review shows, in spite of the large volume of research on the miscible displacement flows, very few studies have been conducted for the displacement flow in immiscible systems. Also, the flow dynamics in immiscible flows are very different from those of the miscible flows due to the presence of a sharp interface separating the fluids and are associated with interfacial tension. On the other hand, miscible flows are associated with diffusion. Selvam *et al.*[10] compared the stability of immiscible flows (with zero surface tension) with miscible flows and found that miscible flows are stable for any Reynolds number when the viscosity ratio is less than a critical value, unlike the immiscible flows with zero surface tension, which can be unstable for any Reynolds number for any arbitrarily small viscosity gradient. Also in miscible flows, the width of the interfacial region

increases with time even when the diffusion coefficient is very small (this rate is proportional to the inverse of Peclet number), which in turn stabilizes the flow (see Refs. 10 and 45).

Very high computational power is necessary to simulate such interfacial flows as fine grids and long domains are required for the accurate simulation of the interfacial dynamics. The lattice Boltzmann method could be ideal for studying the interfacial flows because of its low computational cost and its ability to track the interface automatically. Some relevant studies of the displacement flows are reviewed below. The displacement flows of two immiscible liquids were studied by Chin *et al.*,[46] Grosfils *et al.*,[47] Kang *et al.*,[48] and Dong *et al.*[49] via the lattice Boltzmann method. The effects of wettability, surface tension, viscosity ratio, and gravity have been included sequentially. The recent study of Dong *et al.*[49] considered all these parameters. However the formation of the interfacial instabilities, which are the important characteristics of such flows, was not reported by any of the previous studies. This may be due to the low Reynolds number and smaller computational domain considered in the earlier studies.

In the present work, the displacement flow of two immiscible fluids is investigated using a multiphase LBM approach proposed by He and co-workers.[40,42] We have conducted a systematic parametric study to investigate the effects of viscosity ratio, Atwood number, Froude number, and surface tension. As Selvam *et al.*[10] found that in core-annular flows beyond a critical viscosity ratio, the flow is unstable even when the less viscous fluid is at the wall, we investigated what will happen when a high viscous fluid displaces a less viscous one (a classically stable system) at high viscosity ratio. The effects of angle of inclination on the flow dynamics are also investigated, which have not been studied earlier in the context of immiscible fluids. A linear stability analysis similar to the one of Sahu *et al.*[8] for a three-layer system is compared with the LBM simulations.

The rest of the paper is organized as follows. The problem is formulated in Sec. II, and the results of the lattice Boltzmann simulations are presented in Sec. III. In Sec. IV, we discuss the results of the linear stability analysis, and provide concluding remarks in Sec. V.

II. FORMULATION

Consider a two-dimensional channel initially filled with a stationary, Newtonian, incompressible fluid of viscosity μ_2 and density ρ_2 (fluid "2"). Through an imposed pressure-gradient, this initially filled liquid is displaced by another immiscible liquid of viscosity μ_1 and density ρ_1 (fluid "1"), as shown in Fig. 1. We use a rectangular coordinate system (x, y) to model the flow dynamics, where x and y denote the coordinates in axial and the wall normal directions, respectively. The channel inlet and outlet are located at $x = 0$ and L, respectively. The prescribed boundary conditions are such that fluid can only enter and leave the channel through the inlet and outlet, respectively. The rigid and impermeable walls of the channel are located at $y = 0$ and H, respectively. The aspect ratio of the channel, L/H, is 48. θ is the angle of inclination measured with the horizontal. g is acceleration due to gravity; the two components of the gravity $g\sin\theta$ and $g\cos\theta$ act in the axial and transverse directions, respectively.

A. Numerical method

The simulations are performed with a two-phase lattice Boltzmann method previously reported by Sahu and Vanka,[43] modified to account for unequal dynamic viscosities of the fluids. The methodology is briefly described below. Two evolution equations for the index distribution function (f) and the pressure distribution function (g) are given by

$$\mathrm{f}_\alpha(\mathbf{x}+\mathbf{e}_\alpha\delta\mathrm{t}, \mathrm{t}+\delta\mathrm{t}) - \mathrm{f}_\alpha(\mathbf{x}, \mathrm{t}) = -\frac{\mathrm{f}_\alpha(\mathbf{x}, \mathrm{t}) - \mathrm{f}_\alpha^{\mathrm{eq}}(\mathbf{x}, \mathrm{t})}{\tau} - \frac{2\tau-1}{2\tau}\frac{(\mathbf{e}_\alpha-\mathbf{u})\cdot\nabla\psi(\phi)}{\mathrm{c_s^2}}\Gamma_\alpha(\mathbf{u})\delta\mathrm{t}, \tag{1}$$

$$\mathrm{g}_\alpha(\mathbf{x}+\mathbf{e}_\alpha\delta\mathrm{t}, \mathrm{t}+\delta\mathrm{t}) - \mathrm{g}_\alpha(\mathbf{x}, \mathrm{t}) = -\frac{\mathrm{g}_\alpha(\mathbf{x}, \mathrm{t}) - \mathrm{g}_\alpha^{\mathrm{eq}}(\mathbf{x}, \mathrm{t})}{\tau} +$$

$$\frac{2\tau-1}{2\tau}(\mathbf{e}_\alpha-\mathbf{u})\cdot\Big[\Gamma_\alpha(\mathbf{u})(F_s+\mathbf{G}) - (\Gamma_\alpha(\mathbf{u})-\Gamma_\alpha(0))\nabla\psi(\rho)\Big]\delta t, \tag{2}$$

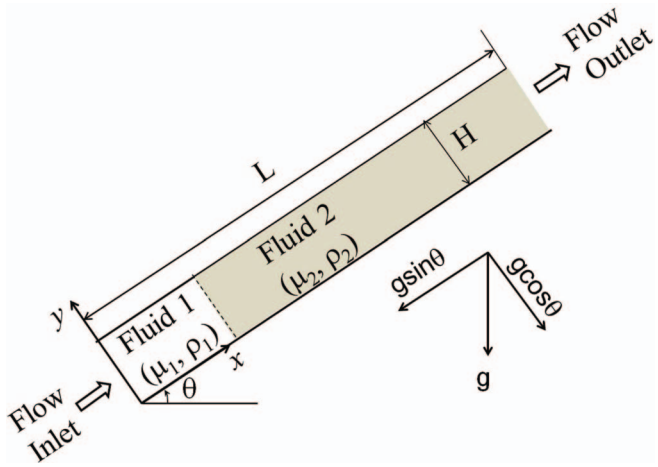

FIG. 1. Schematic showing the geometry (not to scale) and initial flow configuration. The inlet and outlet are located at $x = 0$ and $x = L$, respectively. The aspect ratio of the channel, L/H, is 48. Initially, the channel is filled with fluids "1" and "2" from $0 \le x \le 5$ and $5 \le x \le L$ of the channel, respectively.

where

$$\Gamma_\alpha(\mathbf{u}) = t_\alpha \left[1 + \frac{\mathbf{e}_\alpha \cdot \mathbf{u}}{c_s^2} + \frac{(\mathbf{e}_\alpha \cdot \mathbf{u})^2}{2c_s^4} - \frac{\mathbf{u}^2}{2c_s^2} \right]. \tag{3}$$

Here, $\mathbf{u} = (u, v)$ represents the two-dimensional velocity field; u and v denote velocity components in the x and y directions, respectively; δt is the time step; τ is the single relaxation time using the Bhatnagar-Gross-Krook (BGK) model.[50] The kinematic viscosity, ν is related to the relaxation time by the expression $\nu = (\tau - 1/2)\delta t c_s^2$.

The evolution equations are simulated with a two-dimensional nine-velocity model ($D2Q9$), where

$$e_\alpha = \begin{cases} 0, & \alpha = 0 \\ \left[\cos\left(\frac{(\alpha-1)\pi}{2}\right), \sin\left(\frac{(\alpha-1)\pi}{2}\right)\right], & \alpha = 1, 2, 3, 4 \\ \sqrt{2}\left[\cos\left(\frac{(\alpha-5)\pi}{2} + \frac{\pi}{4}\right), \sin\left(\frac{(\alpha-5)\pi}{2} + \frac{\pi}{4}\right)\right], & \alpha = 5, 6, 7, 8. \end{cases} \tag{4}$$

The weighing coefficients, t_α are given by

$$t_\alpha = \begin{cases} 4/9, & \alpha = 0 \\ 1/9, & \alpha = 1, 2, 3, 4 \\ 1/36, & \alpha = 5, 6, 7, 8. \end{cases} \tag{5}$$

Here, α is the component of the distribution function in the lattice. The equilibrium distribution functions, f_α^{eq} and g_α^{eq} are given by

$$\mathrm{f}_\alpha^{eq} = t_\alpha \phi \left[1 + \frac{\mathbf{e}_\alpha \cdot \mathbf{u}}{c_s^2} + \frac{(\mathbf{e}_\alpha \cdot \mathbf{u})^2}{2c_s^4} - \frac{\mathbf{u}^2}{2c_s^2} \right] \quad \text{and} \tag{6}$$

$$\mathrm{g}_\alpha^{eq} = t_\alpha \left[p + \rho c_s^2 \left(\frac{\mathbf{e}_\alpha \cdot \mathbf{u}}{c_s^2} + \frac{(\mathbf{e}_\alpha \cdot \mathbf{u})^2}{2c_s^4} - \frac{\mathbf{u}^2}{2c_s^2} \right) \right], \tag{7}$$

where $c_s^2 = 1/3$. The index function (ϕ), pressure (p), and velocity field ($\mathbf{u}$) are calculated using

$$\phi = \sum \mathrm{f}_\alpha, \tag{8}$$

$$p = \sum \mathrm{g}_\alpha - \frac{1}{2}\mathbf{u} \cdot \nabla\psi(\rho)\delta t, \tag{9}$$

$$\rho \mathbf{u} c_s^2 = \sum \mathbf{e}_\alpha g_\alpha + \frac{c_s^2}{2}(\mathbf{F_s} + \mathbf{G})\delta t. \tag{10}$$

The fluid density and kinematic viscosity are calculated from the index function as

$$\rho(\phi) = \rho_2 + \frac{\phi - \phi_2}{\phi_1 - \phi_2}(\rho_1 - \rho_2), \tag{11}$$

$$\nu(\phi) = \nu_2 + \frac{\phi - \phi_2}{\phi_1 - \phi_2}(\nu_1 - \nu_2), \tag{12}$$

where ν_1 and ν_2 are the kinematic viscosities of fluid "1" and "2," respectively. ϕ_1 and ϕ_2 are minimum and maximum values of the index function; in the present study, ϕ_1 and ϕ_2 are given values of 0.02381 and 0.2508, respectively.[42]

We use the following expression of $\psi(\phi)$ using the Carnahan-Starling fluid equation of state, which describes the process of phase separation for non-ideal gases and fluids:[51–55]

$$\psi(\phi) = c_s^2 \phi \left[\frac{1 + \phi + \phi^2 - \phi^3}{(1-\phi)^3} - 1 \right] - a\phi^2, \tag{13}$$

where a determines the strength of molecular interactions. The gradient of $\psi(\phi)$ described the physical intermolecular interactions for non-ideal gases or dense fluids. This term plays a key role in separating the phases. A fourth order compact scheme is used to discretize $\nabla\psi$.[56]

The surface tension force (F_s) and gravity forces ($\mathbf{G}$) are given by

$$F_s = \kappa\phi\nabla\nabla^2\phi \quad \text{and} \quad \mathbf{G} = (\rho - \rho_m)g, \tag{14}$$

where κ is the magnitude of surface tension and $\rho_m \equiv (\rho_1 + \rho_2)/2$. The surface tension, σ can be related to κ as follows:[57]

$$\sigma = \kappa \int \left(\frac{\partial \phi}{\partial \zeta} \right)^2 d\zeta = \kappa I(a), \tag{15}$$

where ζ is the direction normal to the interface, and $I(a)$ is given by[42]

$$I(a) = \frac{0.1518(a - a_c)^{1.5}}{1 + 3.385(a - a_c)^{0.5}}, \tag{16}$$

wherein the critical value of Carnahan-Starling equation of state, $a_c = 3.53374$. If $a > a_c$, both the fluids will remain immiscible. Thus, a is chosen to be 4 in the present study.

The hydrodynamic boundary conditions based on the ghost fluid approach are used to simulate the boundaries and equilibrium distribution functions.[43] A Neumann boundary condition for pressure is used at the outlet, while a constant pressure-gradient obtained from the constant volumetric flow rate condition is imposed at the inlet. In addition, the non-equilibrium distribution functions are extrapolated and added to get the instantaneous distribution functions. The various dimensionless parameters describing the flow characteristics are the Atwood number, $At(\equiv (\rho_2 - \rho_1)/(\rho_2 + \rho_1))$, the Reynolds number, $Re(\equiv Q\rho_1/\mu_1)$, the Froude number, $Fr(\equiv Q/H\sqrt{AtgH})$, the capillary number, $Ca(\equiv Q\mu_1/\sigma H)$, and the viscosity ratio, $m = \mu_2/\mu_1$. Here, Q is the volumetric flow rate per unit length in the spanwise direction; in the present study, the characteristic velocity is chosen such that the value of Q is 1.92. The dimensionless time is defined as $t = H^2/Q$.

To accelerate the computational efficiency, the algorithm was implemented on a graphics processing unit (GPU), which has recently become powerful and convenient to use. Our GPU based multiphase lattice Boltzmann solver provides a speed-up factor of 25 as compared to a corresponding central processing unit (CPU) based solver.[58]

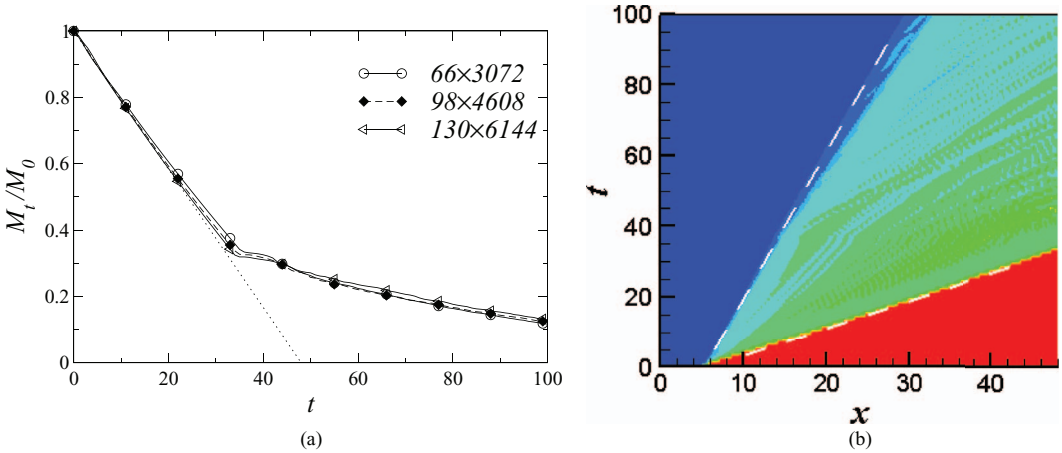

FIG. 2. (a) Variation of volume fraction of the displaced fluid (M_t/M_0) with time obtained using different mesh densities, and (b) the spatio-temporal diagram of $\int_0^H \phi dy$ in time versus x plane for $At = 0.2$, $m = 2$, $Fr = 2.236$, $Re = 100$, $Ca = 0.263$, and $\theta = 45^\circ$. The dotted line in panel (a) represents the analytical solution of the plug-flow displacement, given by $M_t/M_0 = 1 - tH/L$.

III. RESULTS AND DISCUSSION

A. Grid independency test

We begin presenting our results in Fig. 2(a) by first plotting the temporal variation of the dimensionless volume of fluid "2," M_t/M_0, for $At = 0.2$, $m = 2$, $Fr = 2.236$, $Re = 100$, $Ca = 0.263$, and $\theta = 45^\circ$. Here, M_t is defined as $\int_0^L \int_0^H \frac{\phi-\phi_1}{\phi_2-\phi_1} dxdy$. Thus, M_0 denotes the volume of fluid "2" initially occupying the channel ($M_0 \equiv \frac{\phi-\phi_1}{\phi_2-\phi_1} LH$). The parameter values are chosen to correspond to a situation where a heavier fluid is displaced by a fluid of lower density and viscosity. In this case, one would expect the flow to be destabilized because of viscosity contrast and via a Rayleigh-Taylor (RT) instability. Inspection of Fig. 2(a) reveals that M_t/M_0 undergoes an almost linear decrease at the earlier stages of the flow due to its displacement by fluid "1." The slope of the curve during this linear stage is close to that of the line represented by $1 - tH/L$ corresponding to a plug flow displacement of fluid "2" with a sharp vertical interface separating the fluids. This is expected due to the conservation of mass of the fluids entering and leaving the channel. Previously in a miscible system, Sahu *et al.*[32] observed that the slope of M_t/M_0 versus time plot is steeper than that of the plug flow line ($1 - tH/L$), i.e., the actual displacement rate is higher than that of the plug flow. This is attributed to the miscibility effects. In miscible system along with the removal of fluid from the outlet, the flow is associated with phase change of fluid "2" to fluid "1" (which does not occur in immiscible flows). Thus, the displacement rate in the present study is slower than that of miscible flows.[32] At approximately $t = 38$ when the "front" of the displacing fluid "1" reaches the end of simulation domain, as shown in Fig. 3, a transition to a different linear regime occurs; the slope of the M_t/M_0 variation in this regime is much smaller than in the first period, indicating slower displacement process. Also shown in Fig. 2(a) are results with different grids, which demonstrate convergence upon mesh refinement.

The spatio-temporal diagram of $\int_0^H \phi dy$ in time versus x plane is plotted in Fig. 2(b) for the 4608×98 grid. The spatio-temporal diagrams generated using 3072×66 and 6144×130 grids look the same as that shown in Fig. 2(b). It can be seen that the positions of the leading and the trailing "fronts" separating the two fluids exhibit a linear dependence on time. The slopes of the bottom and top white dashed lines represent the velocity of leading (V_l) and trailing (V_t) fronts, respectively. The front velocities obtained using different sets of lattice points are then compared in Table I. It is evident upon the inspection of Table I that the results of the three grids are nearly the same. We chose the 4608×98 grid for the rest of the calculations balancing accuracy and computational time.

TABLE I. The velocity of the leading (V_l) and trailing (V_t) fronts for different grid densities. The rest of the parameter values are $At = 0.2$, $m = 2$, $Fr = 2.236$, $Re = 100$, $Ca = 0.263$, and $\theta = 45^\circ$.

Grid	V_l	V_t
3072×66	1.3141	0.2444
4608×98	1.3139	0.2441
6144×130	1.3132	0.2440

The flow dynamics is illustrated in Fig. 3, which shows the spatio-temporal evolution of the ϕ contours for the parameters as in Fig. 2. The observed flow dynamics is a result of the competition between the imposed pressure-gradient and the axial component of gravity. For the positive angle of inclination considered in the present study, these two forces act in opposite directions. The pressure-driven flow induces motion of fluid "1" into the channel, which is opposed by the acceleration of fluid "2" by the $g\sin\theta$ component of the gravity. On the other hand, the component of the gravitational force in the transverse direction, proportional to $g\cos\theta$, acts to segregate the two fluids. This force therefore counteracts the effects caused by the pressure-gradient and the component of the gravitational force in the axial direction. For the set of parameter values considered in this figure, the effects of the gravity component in the transverse direction ($g\cos\theta$) is quite less as compared to the imposed flow. In other words, as the Fr is relatively larger, the gravitational effects are dominated by the inertial force. Thus, the remnants of fluid "2" left behind by the penetrating finger form thin layers adjacent to the upper and lower walls. The lower layer is thicker than the upper one since the denser, fluid "2" expectedly settles on the lower channel wall. However, for a smaller value of Fr (i.e., for significant gravity effects), we show later that a two-layer flow develops, where the top and bottom parts of the channel are filled with the lighter and heavier fluids, respectively. It can be seen in Fig. 3 that the flow is accompanied by the development of the interfacial instabilities of sawtooth-like shape for $t > 10$. We also observed that the top layer moves faster than the bottom layer. The effects of viscosity contrasts (m), Atwood number (At), and the Froude number (Fr) in a horizontal channel (setting $\theta = 0$) are discussed in Sec. III B.

B. Horizontal channel

In this section, we first discuss the effects of viscosity contrast on the flow dynamics in the case of a horizontal channel. In Figs. 4(a) and 4(b), the temporal evolutions of the dimensionless measure of the volume of fluid "2," M_t/M_0 for different values of m, are plotted for $At = 0$, $Fr = \infty$ (i.e., in the absence of density contrast and gravity), and $At = 0.3$, $Fr = 0.577$, respectively. The rest of the parameter values are $Re = 100$, $Ca = 0.263$, and $\theta = 0^\circ$. It can be seen in Figs. 4(a)

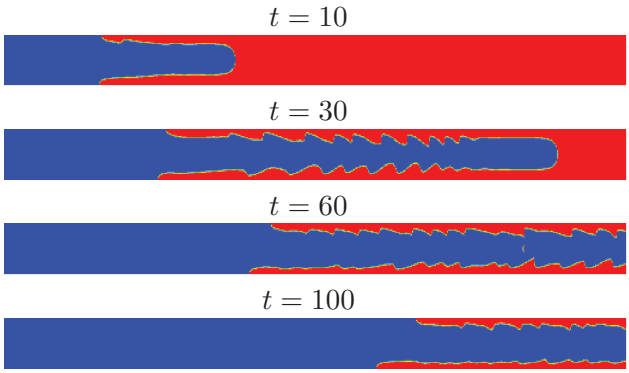

FIG. 3. Spatio-temporal evolution of the contours of the index function, ϕ for $At = 0.2$, $m = 2$, $Fr = 2.236$, $Re = 100$, $Ca = 0.263$, and $\theta = 45^\circ$.

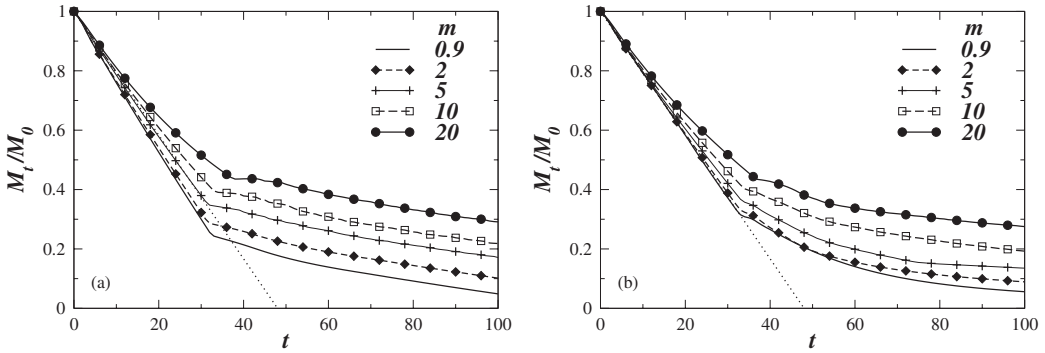

FIG. 4. Variation of volume fraction of the displaced fluid (M_t/M_0) with time for different values of viscosity ratio, m for (a) $At = 0$ and $Fr = \infty$, and (b) $At = 0.3$, $Fr = 0.577$. The rest of the parameters are $Re = 100$, $Ca = 0.263$, and $\theta = 0°$. The dotted lines in panels (a) and (b) represent the analytical solution of plug-flow displacement, given by $M_t/M_0 = 1 - tH/L$.

and 4(b) that increasing the value of m decreases the displacement rate. The dotted lines in Figs. 4(a) and 4(b) represent the analytical solution (given by $M_t/M_0 = 1 - tH/L$), which is obtained when fluid "1" displaces fluid "2" as a plug, without forming a finger-like structure. Inspection of Fig. 4 reveals that for low viscosity ratio, the slope of the curve in the linear region (for $t < 35$ for this set of parameter values) is nearly the same as that of the plug-flow displacement. At approximately $t = 35$, a transition to another linear regime occurs. The displacement rate for $t \geq 35$ decreases significantly as the thin layers of the remnants of fluid "2" at the top and bottom of the channel take longer time to be displaced.

The variations of velocity of the leading (V_l) and trailing (V_t) fronts with viscosity contrasts are shown in Figs. 5(a) and 5(b), respectively. The rest of the parameter values are the same as those used to generate Fig. 4. It can be seen in Figs. 5(a) and 5(b) that m has a non-monotonic effect on the velocity of the leading front, i.e., increasing m increases V_l for $m \leq 5$, a further increase in m leads to a decrease in the value of V_l. This is in contrast to the miscible system, where the velocity of the leading front increases with increasing m (see Sahu *et al.*[3]). It can be seen in Fig. 5(b) that the velocity of the trailing front (V_t) decreases with increasing the viscosity contrasts. This is similar to the finding of Redapangu *et al.*[58] who studied the buoyancy-driven flow of two immiscible fluids in a confined inclined channel. Close inspection of Fig. 5 also reveals that the velocity of the leading front in the presence of density contrasts and gravity is higher than that of the no gravity case. However, the velocity of the trailing front (V_t) is smaller in the presence of density contrasts and gravity. This is expected as the gravity acting in the downward direction settles the remnants of fluid "2" at the bottom part of the channel and opposes the motion in the positive axial direction.

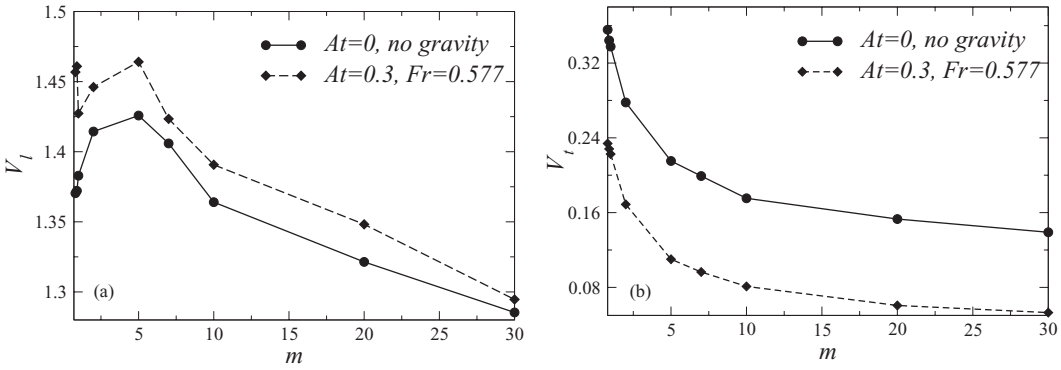

FIG. 5. Variations of velocities of (a) the leading (V_l) and (b) the trailing (V_t) fronts with viscosity ratio, m. The rest of the parameter values are $Re = 100$, $Ca = 0.263$, and $\theta = 0°$.

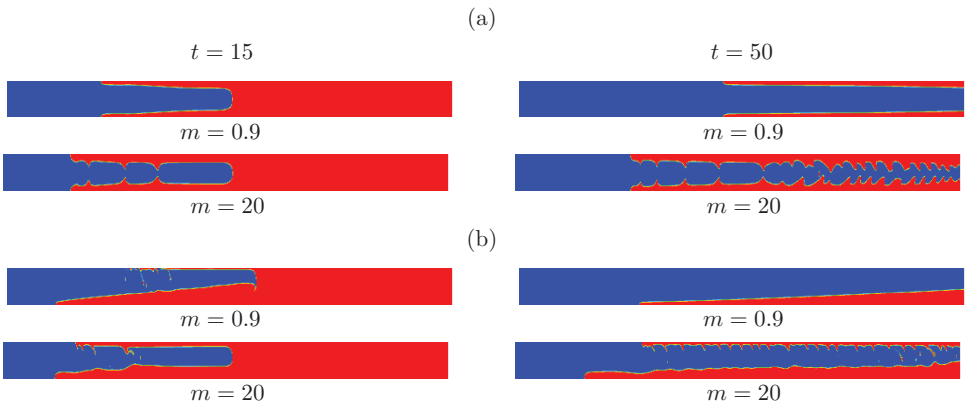

FIG. 6. The contours of the index function, ϕ at $t = 15$ and $t = 50$ in a horizontal channel ($\theta = 0^\circ$) for two different values of viscosity ratio, m for (a) $At = 0$ and $Fr = \infty$ and (b) $At = 0.3$ and $Fr = 0.577$. The rest of the parameter values are $Re = 100$ and $Ca = 0.263$.

In Fig. 6, we plot the evolution of the ϕ contours for different values of m at $t = 15$ and $t = 50$. These two instances of time are considered in order to understand the flow dynamics in the two distinct linear regimes, as shown in Fig. 4. In the absence of density contrast, it can be seen in Fig. 6(a) that for ($m = 0.9$), the flow is fairly stable as in this case a high viscous fluid displaces a less viscous one (this is a stable configuration; see Refs. 1 and 59). For $m = 20$, which represents a situation where less viscous fluid displaces a high viscous fluid, the flow becomes considerably unstable accompanied by a wavy interface. This is purely due to the viscosity stratification. As expected, it can also be seen that the "finger" of the displacing fluid is axially symmetrical in the absence of gravity (see Fig. 6(a)). On the other hand, for $Fr = 0.577$, the "finger" of fluid "1" penetrates into the region of fluid "2" with a blunt "nose" (see Fig. 6(b)). Unlike Fig. 6(a), it can be seen in Fig. 6(b) that the flow becomes unstable due to the RT mechanism even for $m = 0.9$. This "finger" becomes asymmetric: the thickness of the remnants of fluid "2" adjoining the lower wall is larger than that near the upper wall. For $m = 0.9$, the remnants of fluid "2" completely move to the bottom part of the channel at the later times destroying the finger-like structure. The observed asymmetry is brought about by the density contrasts characterized by $At = 0.3$.

C. Inclined channel

Next, we study the effect of inclination angle (θ) on the displacement process. In Fig. 7, the ϕ field at $t = 30$ is plotted for different angles of inclinations. The rest of the parameter values are $m = 10$, $At = 0.2$, $Fr = 1$, $Re = 100$, and $Ca = 0.263$. The gravity is acting in the vertical direction; thus, the two components of the gravity $g\sin\theta$ and $g\cos\theta$ act in the negative axial and negative transverse directions, respectively. It can be seen that the pressure-driven flow induces motion of a "finger" of the less dense and less viscous fluid (fluid "1") into the more dense and more viscous fluid (fluid "2"). This is opposed by the flow due to gravitational force in axial direction, which accelerates fluid "2" into fluid "1" in the downward direction. At the same time, the component of the gravitational force in the transverse direction segregates the two fluids. As the "finger" of fluid "1" penetrates into fluid "2," the remnants of fluid "2" left behind form thin layers adjacent to the upper and lower walls, and a two-layer structure is obtained. The interface separating the two fluids becomes unstable forming Yih-type instabilities. The linear stability characteristics of this two-layer flow will be examined in Sec. IV.

In a horizontal channel ($\theta = 0^\circ$), the transverse component of gravity becomes maximum and the axial penetration is only due to the imposed pressure-gradient. In this case, the high density fluid (remnants of fluid "2") tries to segregate from the less dense fluid (fluid "1") by moving in the transverse direction into the bottom part of the channel. As a result, the lower layer becomes thicker than the upper layer, resulting in an asymmetric "finger" moving in the axial direction. Comparison

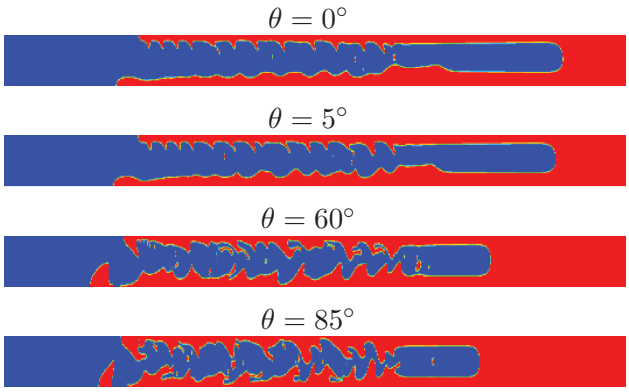

FIG. 7. The contours of the index function, ϕ at $t = 30$ for different inclination angles. The rest of the parameter values are $m = 10$, $At = 0.2$, $Fr = 1$, $Re = 100$, and $Ca = 0.263$.

with Fig. 6, which corresponds to a smaller value of *Fr* reveals that the thickness of the lower layer increases with decreasing *Fr*. This is expected as decreasing *Fr* for a given inclination increases the gravitational influence in the transverse direction, which increases the segregation of the fluids. It can be seen in Fig. 7 that increasing θ for a given value of *Fr* also decreases fluid segregation due to the diminishing role of the gravitational force. Therefore, the finger becomes increasingly symmetrical with increasing the angle of inclination (see Fig. 7). This also increases the intensity of the interfacial instabilities, which in turn increases the removal rate of fluid "2" in later times (for $t > 60$ for this set of parameter values), as shown in Fig. 8.

The spatio-temporal diagrams of $\int_0^H \phi dy$ in time versus x plane are plotted in Fig. 9 for different angles of inclination, with the rest of the parameter values kept the same as Fig. 7. It can be seen that the speed of the trailing front decreases with increasing the value of θ. This happens because increasing θ increases the gravitational influence ($g\sin\theta$) in the negative axial direction. We found that a further increase in the gravitational force by decreasing the value of *Fr* leads the heavier fluid in the lower layer to move in the opposite direction.[60] It can also be seen that the variation of the location of the leading front tip, x_{tip} is nonlinear for larger angle of inclinations, and this nonlinearity is predominant at later times. In contrast, Sahu *et al.*[32] observed a constant slope in the x_{tip} versus time plot. However, their study was associated with miscible fluids, in which diffusion may have played a role to reduce the nonlinearity observed in the present study.

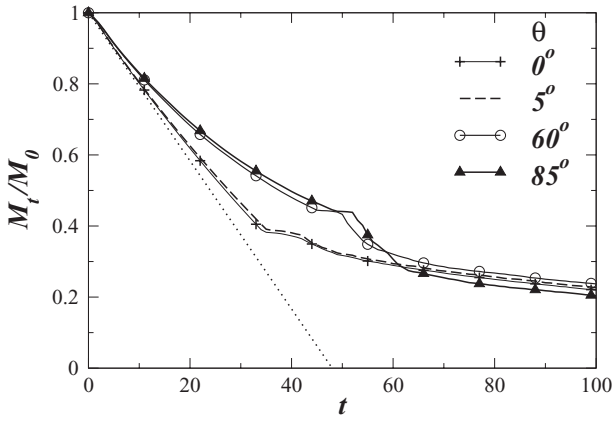

FIG. 8. The effects of angle of inclination on the variation of the volume fraction of the displaced fluid, (M_t/M_0) with time. The parameters used are $m = 10$, $At = 0.2$, $Fr = 1$, $Re = 100$, and $Ca = 0.263$. The dotted line represents the analytical solutions of the variation of M_t/M_0 for plug-flow displacement, given by $M_t/M_0 = 1 - tH/L$.

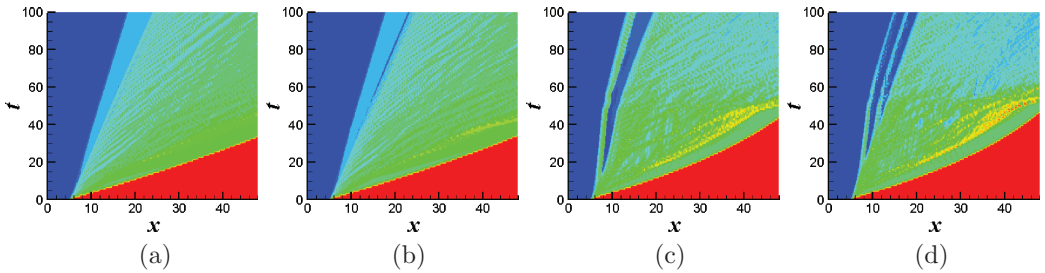

FIG. 9. The spatio-temporal diagram of $\int_0^H \phi dy$ in time versus x plane for (a) $\theta = 0^\circ$, (b) $\theta = 5^\circ$, (c) $\theta = 60^\circ$, and (d) $\theta = 85^\circ$. The rest of the parameter values are the same as those in Fig. 7.

Figure 10 shows the vorticity (first panel) and velocity vectors (second panel) fields for the parameter values the same as those used to generate Fig. 7. It can be seen that the central region contains strong vortical activity. Inspection of Fig. 10 also reveals that the level of vortical structures in the central region increases with increasing the angle of inclination as the flow accelerates due to the combined action of the pressure-gradient and the components of the gravity.

The effect of viscosity contrast is investigated in Fig. 11, where we show contours of the index function, ϕ at different times for different viscosity ratios. It can be seen in Fig. 11(a) that the flow for $m < 1$ is associated with the formation of small scale structures. It is well known that flow for

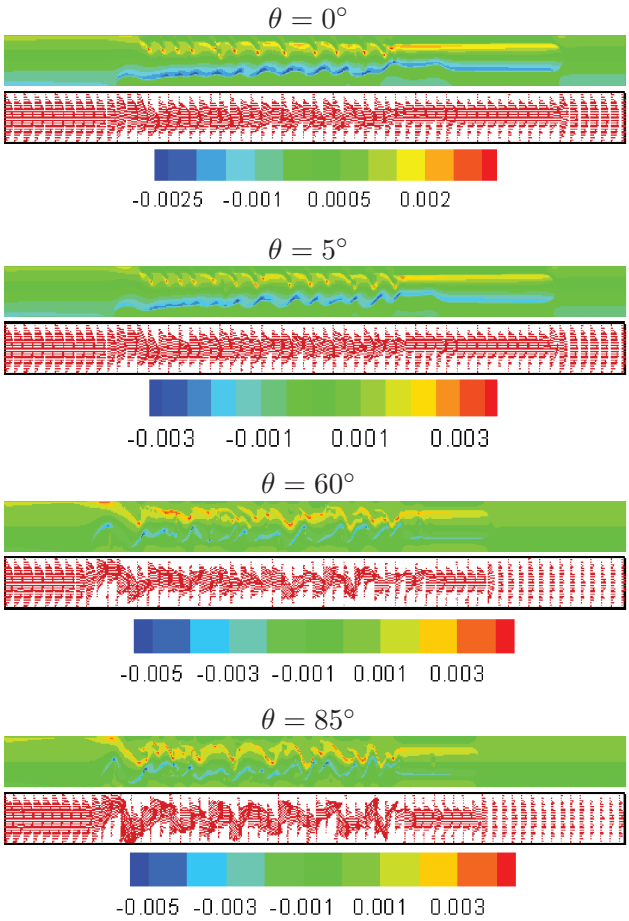

FIG. 10. The vorticity (first panel) and velocity vectors (second panel) fields for the same parameter values as those used to generate Fig. 7. The color-maps for the vorticity contours are shown as third panel.

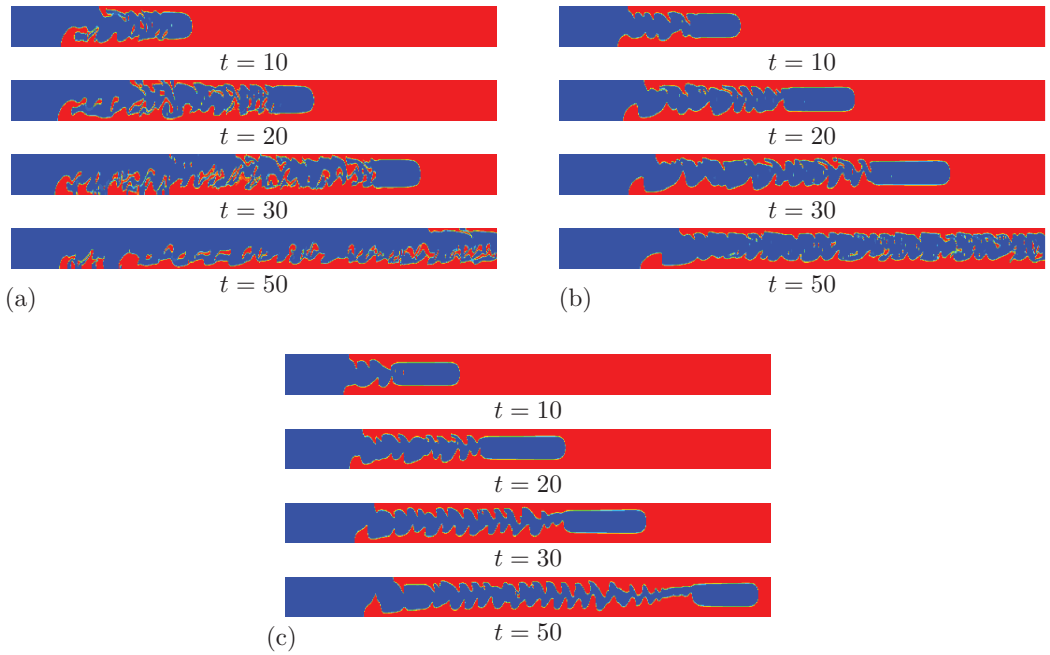

FIG. 11. Spatio-temporal evolution of contours of the index function, ϕ for (a) $m = 0.8$, (b) $m = 10$, and (c) $m = 30$. The rest of the parameters are $At = 0.2$, $Fr = 1$, $Re = 100$, $\theta = 45^\circ$, and $Ca = 0.263$.

$m < 1$ is stable without density contrast and gravity[1,59] (also see Fig. 6). Thus, instabilities in this case are due to the RT mechanism as the high dense fluid moves in the negative axial direction while the finger of fluid "1" penetrates inside the channel due to the imposed pressure gradient. The back flow of the denser fluid is clearly evident in Fig. 12(a), where the spatio-temporal diagram of $\int_0^H \phi dy$ is plotted in time versus x plane. It can be seen in Fig. 11 that the flow becomes more coherent with increasing viscosity ratio. Inspection of Figs. 12(b) and 12(c) also reveals that there is no back flow for higher viscosity ratio. Thus, the rate of displacement of fluid "2" also decreases with increase in viscosity ratio, as shown in Fig. 13.

In Fig. 14, we investigate the effect of surface tension on the ϕ fields at $t = 30$ by considering three values of capillary number, Ca. The rest of the parameter values used to generate this plot are $m = 5$, $At = 0.2$, $Fr = 1$, $Re = 100$, and $\theta = 45^\circ$. Inspection of Fig. 14 reveals that the surface tension makes the flow dynamics coherent by stabilizing the short wavelength waves,[4] and decreasing value of Ca, which corresponds to increase in surface tension, increases the stabilizing influence of the flow.

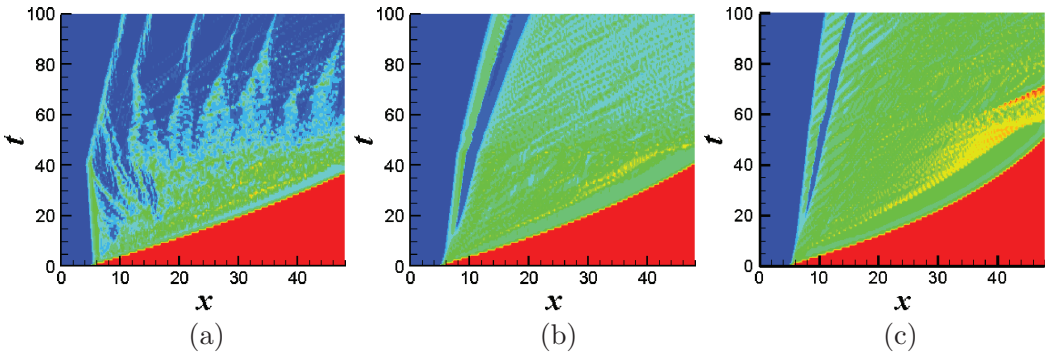

FIG. 12. The spatio-temporal diagram of $\int_0^H \phi dy$ in time versus x plane for (a) $m = 0.8$, (b) $m = 10$, and (c) $m = 30$. The rest of the parameter values are the same as those used to generate Fig. 11.

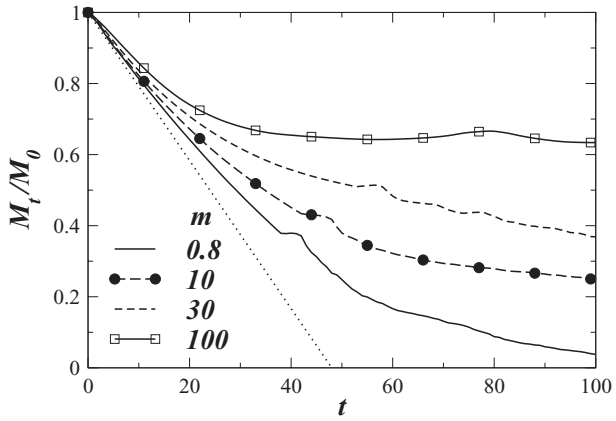

FIG. 13. Effects of viscosity ratio, m on variation of the volume fraction of the displaced fluid, (M_t/M_0) with time. The rest of the parameter values are the same as those used to generate Fig. 11. The dotted line represents the analytical solution for plug-flow displacement, given by $M_t/M_0 = 1 - tH/L$.

We next study the effects of Froude number in a near horizontal channel ($\theta = 5°$). Figures 15(a) and 15(b) show the variation of the normalized front velocity, FrV_l with Froude number, Fr for $m = 1$ and $m = 10$, respectively. Two values of Atwood number, $At = 0.2$ and 0.04 are considered. The rest of the parameter values are $Re = 100$ and $Ca = 0.263$. It can be seen in Figs. 15(a) and 15(b) that the results for both the values of At collapse on a single curve; these are also independent of viscosity ratio. This suggests that for the parameter values considered, the velocity of the leading front can be obtained by balancing the buoyancy (proportional to $(\rho_2 - \rho_1)g$) and imposed pressure force with the inertial force. The dashed lines in Figs. 15(a) and 15(b) represent the best fitted polynomial, given by $FrV_l = 0.38 + 0.665Fr + 0.3534Fr^2$. The first and second terms on the right hand side correspond to the buoyancy and imposed pressure forces, respectively. The leading term in the best fit curve compares well with that of Sahu *et al.*,[43] who studied the buoyancy-driven "lock-exchange flow" of two immiscible fluids in an inclined channel and that of Taghavi *et al.*[61] for miscible displacement flow in a near horizontal channel. However, in a purely buoyancy-driven flow of two miscible fluids in an inclined pipe, Séon *et al.*[62] determined the leading term (=0.7) by balancing the buoyancy with the inertial force. This difference in the value of the leading term is attributed to the cylindrical geometry considered by Séon *et al.*[62]

Next, we considered the three points marked with points 1, 2, and 3 in Fig. 15(a), which correspond to $Fr = 0.604$, $Fr = 0.671$, and $Fr = 2.24$, respectively. The spatio-temporal diagrams of $\int_0^H \phi dy$ in x-t plane are plotted for $Fr = 0.604$, $Fr = 0.671$, and $Fr = 2.24$ in Figs. 16(a)–16(c), respectively. The rest of the parameter values are the same as Fig. 15. It can be seen in Fig. 16(a) that the trailing front moves upstream for $0 \le t \le 60$ and then moves in the downstream direction for $t > 60$. This is termed as "temporary back flow" by Taghavi *et al.*[34] For $Fr = 2.24$, it can be seen that

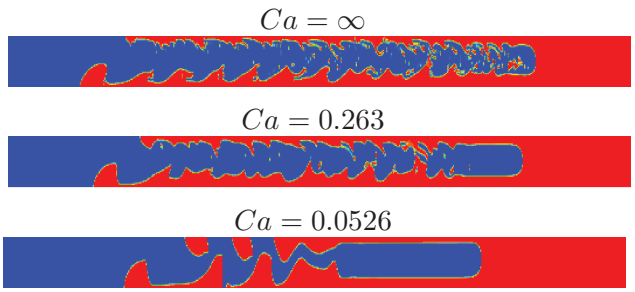

FIG. 14. The contours of the index function, ϕ for different values of capillary number at $t = 30$. The rest of the parameter values are $m = 5$, $At = 0.2$, $Fr = 1$, $Re = 100$, and $\theta = 45°$.

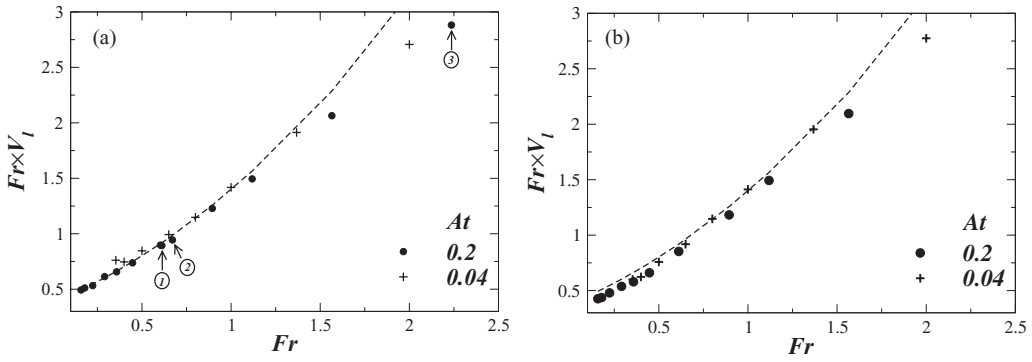

FIG. 15. Variation of the normalized front velocity, FrV_l with Froude number, Fr for (a) $m = 1$, (b) $m = 10$. The rest of the parameter values are $Re = 100$, $Ca = 0.263$, and $\theta = 5^\circ$. The dashed line is the best fitted polynomial, given by $FrV_l = 0.38 + 0.665Fr + 0.3534Fr^2$. The points 1, 2, and 3 in panel (a) correspond to $Fr = 0.604$, $Fr = 0.671$, and $Fr = 2.24$, respectively.

the trailing front moves in the downstream direction for any $t > 0$ ("instantaneous displacement"). It can be observed that $Fr = 0.671$ is a marginal state, where the trailing front becomes stationary for some time before moving in the downstream direction. This is termed as "stationary back flow" by Taghavi *et al.*[34] Thus, for $Fr > 0.671$, a temporary lock-exchange type of flow is observed for this set of parameter values.

As suggested by Taghavi *et al.*,[61] in the exchange flow dominated regime, it is possible to derive a single dimensionless parameter, $\chi(\equiv 2Re\sin\theta/AtFr^2)$ by balancing the buoyancy force in the axial direction with the imposed pressure force. The normalized front velocity $(2V_f/\chi)$ is plotted against $2/\chi$ in Figs. 17(a) and 17(b) for $m = 1$ and 10, respectively. The filled circle in (a) corresponds to $\chi = 193.6$, and the squares below and above this filled circle correspond to $\chi = 293.1$ and $\chi = 17.4$, respectively. It can be seen that for $\chi > \chi_{cr}(= 193.6)$ the results are diverged from the $V_l = V_0$ line, which corresponds to pure displacement flow. For the set of parameter values considered, the value of χ_{cr} corresponds to $Fr = 0.671$ (see Fig. 16(b)). Thus, the trailing front has a tendency to move in the downstream direction (back flow) for $\chi > \chi_{cr}$, whereas it moves only in the positive axial direction for $\chi < \chi_{cr}$ (no back flow). In the case of miscible displacement flows in a near horizontal pipe, Taghavi *et al.*[61] found the value of χ_{cr} to be 116.32. This difference is also due to the cylindrical geometry considered by these authors. The result seems to be invariant for $m = 10$.

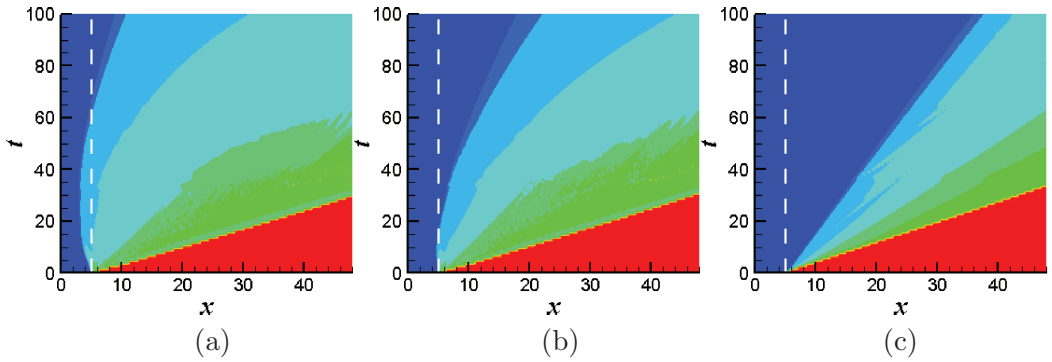

FIG. 16. The spatio-temporal diagram of $\int_0^H \phi dy$ in time versus x plane for (a) $Fr = 0.604$, (b) $Fr = 0.671$, and (c) $Fr = 2.24$ for the parameters $At = 0.2$, $m = 1$, $Re = 100$, $\theta = 5^\circ$, and $Ca = 0.263$. The white dashed lines represent the initial location of the interface ($x = 5$).

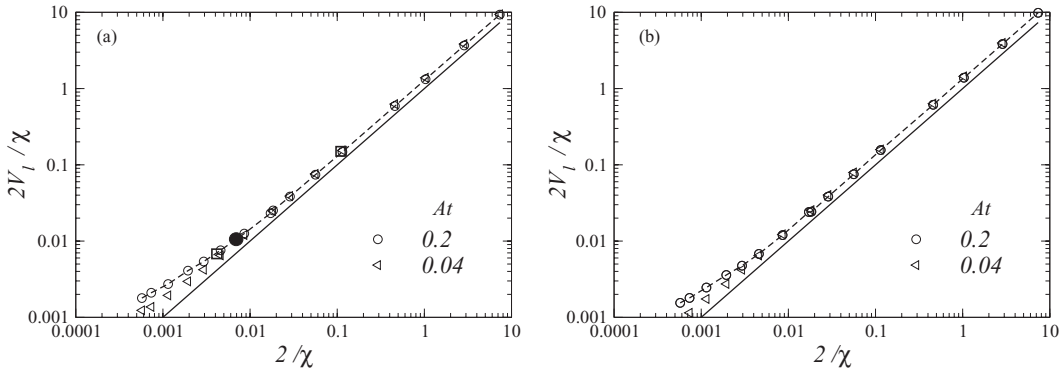

FIG. 17. Normalized front velocity as a function of normalized Fr, for (a) $m = 1$ and (b) $m = 10$ where $\chi = 2Re\sin\theta/AtFr^2$. The rest of the parameters are $Re = 100$, $\theta = 5^\circ$, and $Ca = 0.263$. The solid line represents the line $V_l = V_0$. The filled circle in (a) corresponds to $Fr = 0.671$, the squares to the left and the right of this filled circle correspond to $Fr = 0.604$ and $Fr = 2.24$, respectively.

IV. LINEAR STABILITY ANALYSIS

In this section, the linear stability analysis of the three-layer channel flow, which can be obtained when the elongated "finger" of fluid "1" penetrates into the bulk of fluid "2" (as discussed in Sec. III C), is considered. The base state whose linear stability characteristics will be analyzed corresponds to a parallel, fully-developed flow in which the two fluids are separated by flat interfaces, with fluid "1" located in the region $-h^0 \le y \le h^0$, as shown in Fig. 18. We assume $P_1 = P_2 \equiv P$ and the pressure distribution is linear in x.

By assuming symmetry in the wall-normal direction, the bottom part of the channel is considered for the linear stability analysis. The velocity distribution is given by

$$U_1 = \frac{1}{2}\frac{dP}{dx}y^2 + c_1 y + c_2, \tag{17}$$

$$U_2 = \frac{1}{2m}\frac{dP}{dx}y^2 + \frac{c_3 y}{m} + c_4, \tag{18}$$

$$\text{and} \quad \int_0^h U_1 dy + \int_h^1 U_2 dy = 1. \tag{19}$$

The pressure gradient, dP/dx and the integration constants, c_1, c_2, c_3, and c_4 are obtained using the no-slip condition at the lower wall, symmetric boundary conditions across the channel centerline, and demanding continuity of velocity and stress at the interface. Equation (19) represents a condition

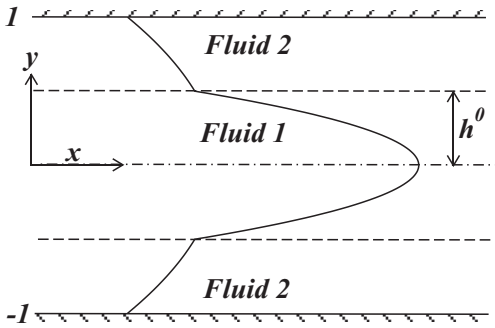

FIG. 18. Schematic showing the geometry and initial condition of the flow. Also shown here is profile of the steady, streamwise velocity component generated with $m = 10$ and $h^0 = 0.5$.

of constant volumetric flow rate, Q, chosen to be one, and the half channel width has been used as a length scale in this section. A typical velocity profile for $m = 10$ and $h^0 = 0.5$ is shown in Fig. 18.

We investigate the stability of the base state characterized by U_1 and U_2 to infinitesimal, two-dimensional (2D) disturbances using a normal mode analysis by expressing each flow variable as the sum of a base state and a 2D perturbation

$$u_k(x, y, t) = U_k(y) + \hat{u}_k(x, y, t), \tag{20}$$

$$v_k(x, y, t) = \hat{v}_k(x, y, t), \quad \text{and} \tag{21}$$

$$p_k(x, y, t) = P + \hat{p}_k(x, y, t) \tag{22}$$

with $(k = 1, 2)$. Similarly, h can be expanded as follows:

$$h(x, t) = h^0 + \hat{h}(x, t), \tag{23}$$

where the superscript "0" designates base state quantities. Substitution of Eqs. (20)–(23) into the Navier-Stokes and continuity equations, subtraction of the base state equations, and subsequent linearisation yield the linear stability equations in terms of primary variables. These equations are then re-expressed in terms of the stream-function, $(u_k, v_k) = (\partial\Psi_k/\partial y, -\partial\Psi_k/\partial x)(k = 1, 2)$ and the decomposition $\Psi(x, y, t) = \Phi(y)e^{\mathrm{i}(\beta x - \omega t)}$ is imposed, whence,

$$\hat{u}_k(x, y, t) = \Phi_k'(y)\mathrm{e}^{\mathrm{i}(\beta x - \omega t)}, \tag{24}$$

$$\hat{v}_k(x, y, t) = -\mathrm{i}\beta\Phi_k(y)\mathrm{e}^{\mathrm{i}(\beta x - \omega t)}, \tag{25}$$

$$\hat{p}_k(x, y, t) = p_k(y)\mathrm{e}^{\mathrm{i}(\beta x - \omega t)}, \quad \text{and} \tag{26}$$

$$\hat{h}(x, t) = \eta e^{\mathrm{i}(\beta x - \omega t)}. \tag{27}$$

Then eliminating the pressure perturbations from the resultant equations, yields the following coupled Orr-Sommerfeld-type equations:

$$\mathrm{i}\beta Re\left[\left(\Phi_1'' - \beta^2\Phi_1\right)(U_1 - c) - \Phi_1 U_1''\right] = \left[\Phi_1'''' - 2\beta^2\Phi_1'' + \beta^4\Phi_1\right], \tag{28}$$

$$\mathrm{i}\beta Re\left(\frac{1 + At}{1 - At}\right)\left[\left(\Phi_2'' - \beta^2\Phi_2\right)(U_2 - c) - \Phi_2 U_2''\right] = m\left[\Phi_2'''' - 2\beta^2\Phi_2'' + \beta^4\Phi_2\right]. \tag{29}$$

Here, the prime represents differentiation with respect to y, and Φ_k and η denote the amplitudes of the streamfunction and interfacial perturbation, respectively; β is a axial real wavenumber, $\omega(\equiv \beta c)$ is a complex frequency, wherein c is a complex phase speed of the disturbance. Note that $(1 + At)/(1 - At)$ represents the density ratio, ρ_1/ρ_2. In the temporal stability analysis considered in this section, $\omega_i > 0$ indicates the presence of a linear instability.

The eigenvalue c and the eigenfunctions Φ_1 and Φ_2 are obtained via solution of Eqs. (28) and (29) subject to the following boundary conditions: the no-slip and no-penetration conditions at the upper wall

$$\Phi_2 = \Phi_2' = 0 \qquad \text{at} \quad y = -1; \tag{30}$$

and either

$$\Phi_1' = \Phi_1''' = 0, \quad \text{or} \quad \Phi_1 = \Phi_1'' = 0 \quad \text{at} \quad y = 0 \quad \text{(centerline)}, \tag{31}$$

which are appropriate for symmetric and antisymmetric modes, respectively. Our results (not shown) reveal that the symmetric mode is dominant for the range of parameters considered in the present work. Consequently, all of the results presented below correspond to symmetric mode exclusively. Using the continuity of the velocity and stress components for the disturbance in the axial and the wall-normal directions at the interface, along with the kinematic boundary condition, we obtained

$$\Phi_1 = \Phi_2, \tag{32}$$

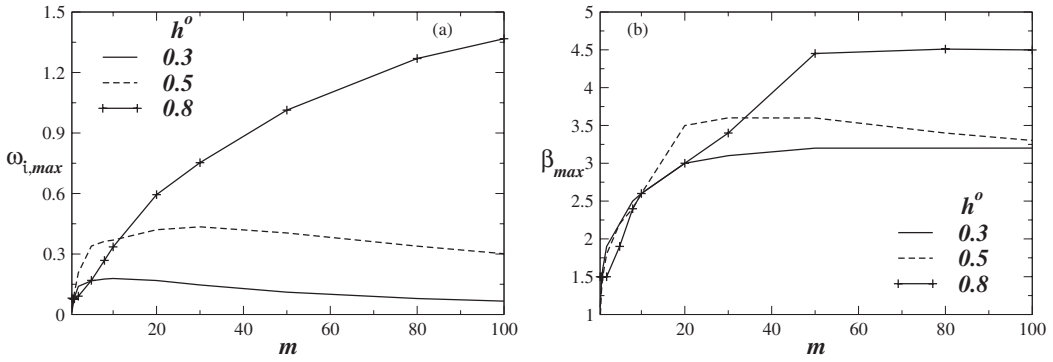

FIG. 19. Variation of (a) maximal growth rate, $\omega_{i,max}$, (b) axial wavenumber associated with the most dangerous mode, β_{max} with viscosity ratio, m. The rest of the parameter values are $Re = 100$, $At = 0.1$, $Fr = 1$, $\theta = 0^\circ$, and $Ca = 0.263$.

$$\Phi_1' - \Phi_2' + \eta\left(U_1' - U_2'\right) = 0, \tag{33}$$

$$m\left(\Phi_2'' + \beta^2\Phi_2\right) - \left(\Phi_1'' + \beta^2\Phi_1\right) + \frac{\left(U_1'' - mU_2''\right)}{(U_1 - c)} = 0, \tag{34}$$

$$-\mathrm{i}\beta Re\left[\Phi_1'(c - U_1) + \Phi_1 U_1'\right] + \mathrm{i}\beta\left(\frac{1 + At}{1 - At}\right) Re\left[\Phi_2'(c - U_2) + \Phi_2 U_2'\right] - \left(\Phi_1''' - \beta^2\Phi_1'\right) +$$

$$m\left(\Phi_2''' - \beta^2\Phi_2'\right) + 2\beta^2\Phi_1' - 2m\beta^2\Phi_2' = \left(\frac{\beta^2}{Ca} + \mathcal{G}\right)\mathrm{i}\beta\frac{\left(\Phi_1' - \Phi_2'\right)}{\left(U_2' - U_1'\right)}, \tag{35}$$

where η is given by

$$\eta = \Phi_1/(c - U_1)\,|_h = \Phi_2/(c - U_2)\,|_h. \tag{36}$$

Here, $\mathcal{G} \equiv 2ReAt^2/Fr^2(At - 1)$. The stability analysis conducted here is similar to the one given in Sahu *et al.*[7,8,63] We recover Eqs. (28)–(36) from the stability equations and boundary conditions given in Sahu *et al.*[8] for Newtonian fluids.

The effects of varying the viscosity ratio (m), Atwood number (At), Froude number (Fr), and capillary number (Ca) on the linear stability characteristics are discussed next. In Fig. 19(a), the variation of the maximal growth rate, $\omega_{i,max}$, and axial wavenumber associated with the most dangerous mode, β_{max} are plotted against the viscosity ratio. It can be seen in Fig. 19(a) that $\omega_{i,max}$ increases and then decreases with increasing the value of viscosity ratio, m. It

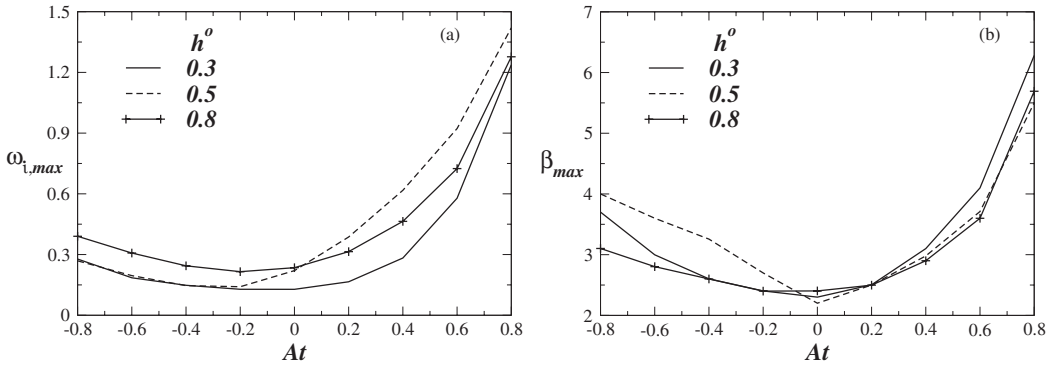

FIG. 20. Variation of (a) maximal growth rate, $\omega_{i,max}$, (b) axial wavenumber associated with the most dangerous mode, β_{max} with Atwood number At. The rest of the parameter values are $Re = 100$, $m = 10$, $Fr = 1$, $\theta = 0^\circ$, and $Ca = 0.263$.

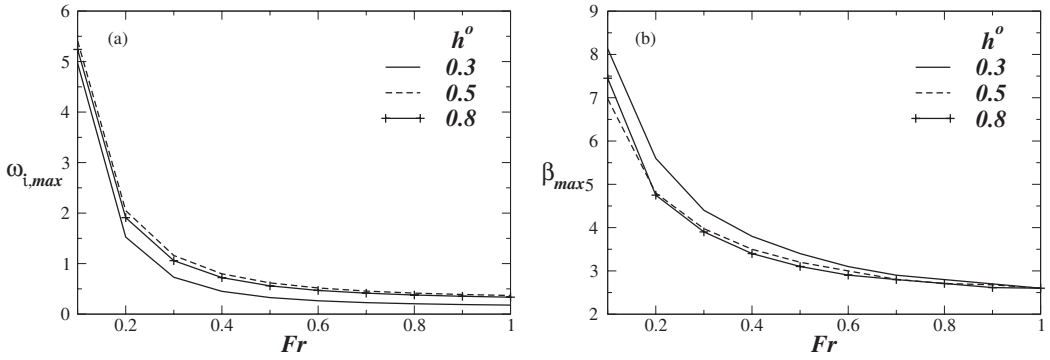

FIG. 21. Variation of (a) maximal growth rate, $\omega_{i,max}$, (b) axial wavenumber associated with the most dangerous mode, β_{max} with Froude number, Fr. The rest of the parameter values are $Re = 100$, $m = 10$, $At = 0.1$, $\theta = 0^\circ$, and $Ca = 0.263$.

can be seen in Fig. 19(b) that the axial wavenumber associated with the most dangerous mode, β_{max} increases with increasing the viscosity ratio. This prediction from the linear stability analysis is in agreement with our numerical simulation results plotted in Figs. 6 and 11. Similarly, the variation of $\omega_{i,max}$ and β_{max} with Atwood number, At are plotted in Figs. 20(a) and 20(b), respectively. Inspection of this figure reveals that the disturbance growth rate is minimum when there is no density contrast, and increasing or decreasing the ratio of the density of the annular to the core fluid increases the growth rate. A similar behavior is also observed for the variation of axial wavenumber of the most dangerous mode with At. It can be seen in Figs. 21 and 22 that $\omega_{i,max}$ and β_{max} monotonically decrease with increasing Froude number and inverse capillary number. The decrease in β_{max} with the inverse capillary number suggests that the wavelength of the most dangerous mode increases with increasing surface tension. A similar result was also obtained by several researchers (e.g., Selvam *et al.*[10]). This behavior can be clearly evident in Fig. 14 where we can see that decreasing Ca (increasing surface tension) reduces the shortwave length small scale structures. An energy budget analysis similar to that given in Sahu *et al.*[8] (not shown) predicts that the most dangerous modes are interfacial ones. Thus, these instabilities are of Yih-type as we do not see any "roll-up" phenomenon in the present study.

V. CONCLUDING REMARKS

In this paper, we have investigated the pressure-driven displacement flow of two immiscible fluids in an inclined channel in the presence of viscosity and density gradients by using a multiphase lattice Boltzmann method algorithm originally proposed by He *et al.*[40,42] The LBM is a simple,

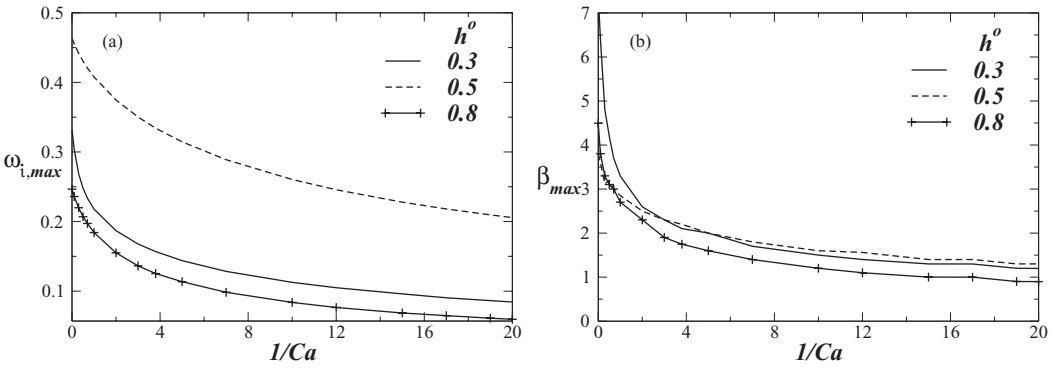

FIG. 22. Variation of (a) maximal growth rate, $\omega_{i,\,max}$, (b) axial wavenumber associated with the most dangerous mode, β_{max} with capillary number, Ca. The rest of the parameter values are $Re = 100$, $m = 10$, $At = 0.1$, $\theta = 0^\circ$, and $Fr = 1$.

elegant, and easy to implement mesoscopic model of fluid flows, sharply in contrast to the nonlinear, coupled Navier-Stokes equations. Although its origins are in simulating compressible flows, it can also be applied for simulating nearly incompressible fluids using a non-ideal equation of state. In the present study, the effects of viscosity ratio, density ratio characterized by Atwood number, gravity characterized by Froude number, and surface tension characterized by capillary number are examined. The effect of channel inclination is investigated in terms of flow structures, front velocities, and displacement rates. Our results indicate that increasing viscosity ratio decreases the displacement rate, and has a non-monotonic effect on the velocity of the leading front. However, the velocity of the trailing edge decreases with increasing the viscosity ratio. We found that the displacement rate of the thin-layers (after the leading front crossed the simulation domain) increases with increasing the angle of inclination. This is due to the increase in the intensity of the interfacial instabilities with increasing the inclination angle, which helps in cleaning the channel. Our results predict the front velocity of the "lock-exchange flow" of two immiscible fluids in the exchange flow dominated regime. This is also consistent with the finding of Taghavi *et al.*[61,62] for the exchange flow of miscible fluids at high Peclet number. A linear stability analysis of a three-layer system predicts the behavior of the numerical simulation qualitatively. We also observe that the instabilities are of Yih-type because of the lack of vortex roll-up.

ACKNOWLEDGMENTS

The support from the Indian Institute of Technology Hyderabad, India, is gratefully acknowledged. We also thank the Department of Science and Technology, India, for their partial financial support. The authors thank Dr. Aaron Shinn for assistance in the GPU implementation of the code.

[1] D. D. Joseph, R. Bai, K. P. Chen, and Y. Y. Renardy, "Core-annular flows," Ann. Rev. Fluid Mech. **29**, 65 (1997).
[2] M. Regner, M. Henningsson, J. Wiklund, K. Östergren, and C. Trägårdh, "Predicting the displacement of yoghurt by water in a pipe using CFD," Chem. Eng. Technol. **30**, 844 (2007).
[3] K. C. Sahu, H. Ding, P. Valluri, and O. K. Matar, "Linear stability analysis and numerical simulation of miscible channel flows," Phys. Fluids **21**, 042104 (2009).
[4] C. S. Yih, "Instability due to viscous stratification," J. Fluid Mech. **27**, 337 (1967).
[5] G. M. Homsy, "Viscous fingering in porous media," Ann. Rev. Fluid Mech. **19**, 271 (1987).
[6] S. G. Yiantsios and B. G. Higgins, "Numerial solution of eigenvalue problems using the compound matrix-method," J. Comp. Phys. **74**, 25 (1988).
[7] K. C. Sahu, P. Valluri, P. D. M. Spelt, and O. K. Matar, "Linear instability of pressure-driven channel flow of a Newtonian and Herschel-Bulkley fluid," Phys. Fluids **19**, 122101 (2007).
[8] K. C. Sahu and O. K. Matar, "Three-dimensional linear instability in pressure-driven two-layer channel flow of a Newtonian and a Herschel-Bulkley fluid," Phys. Fluids **22**, 112103 (2010).
[9] R. Govindarajan, "Effect of miscibility on the linear instability of two-fluid channel flow," Int. J. Multiphase Flow **30**, 1177 (2004).
[10] B. Selvam, S. Merk, R. Govindarajan, and E. Meiburg, "Stability of miscible core-annular flows with viscosity stratification," J. Fluid Mech. **592**, 23 (2007).
[11] S. V. Malik and A. P. Hooper, "Linear stability and energy growth of viscosity stratified flows," Phys. Fluids **17**, 024101 (2005).
[12] K. C. Sahu and R. Govindarajan, "Linear stability of double-diffusive two-fluid channel flow," J. Fluid Mech. **687**, 529 (2011).
[13] M. E. Charles, G. W. Govier, and G. W. Hodgson, "The horizontal pipeline flow of equal density oil-water mixtures," Can. J. Chem. Eng. **39**, 27 (1961).
[14] R. Bai, K. Chen, and D. D. Jospeh, "Lubricated pipelining: Stability of core annular flow. Part 5. Experiments and comparison with theory," J. Fluid Mech. **240**, 97 (1992).
[15] J. Li and Y. Y. Renardy, "Direct simulation of unsteady axisymmetric core-annular flow with high viscosity ratio," J. Fluid Mech. **391**, 123 (1999).
[16] C. Kouris and J. Tsamopoulos, "Dynamics of axisymmetric core-annular flow in a straight tube. I. The more viscous fluid in the core, bamboo waves," Phys. Fluids **13**, 841 (2001).
[17] C. Kouris and J. Tsamopoulos, "Dynamics of axisymmetric core-annular flow in a straight tube. II. The less viscous fluid in the core, saw tooth waves," Phys. Fluids **14**, 1011 (2002).
[18] H. H. Wei and D. S. Rumschitzki, "The weakly nonlinear interfacial stability of a core-annular flow in a corrugated tube," J. Fluid Mech. **466**, 149 (2002).
[19] G. I. Taylor, "Deposition of viscous fluid on the wall of a tube," J. Fluid Mech. **10**, 161 (1961).
[20] B. G. Cox, "On driving a viscous fluid out of a tube," J. Fluid Mech. **14**, 81 (1962).
[21] P. Petitjeans and P. Maxworthy, "Miscible displacements in capillary tubes. Part 1. Experiments," J. Fluid Mech. **326**, 37 (1996).

[22] C.-Y. Chen and E. Meiburg, "Miscible displacement in capillary tubes. Part 2. Numerical simulations," J. Fluid Mech. **326**, 57 (1996).
[23] J. Kuang, T. Maxworthy, and P. Petitjeans, "Miscible displacements between silicone oils in capillary tubes," Eur. J. Mech. B/Fluids **22**, 271 (2003).
[24] E. Lajeunesse, J. Martin, N. Rakotomalala, and D. Salin, "3D instability of miscible displacements in a Hele-Shaw cell," Phys. Rev. Lett. **79**, 5254 (1997).
[25] E. Lajeunesse, J. Martin, N. Rakotomalala, D. Salin, and Y. C. Yortsos, "Miscible displacement in a Hele-Shaw cell at high rates," J. Fluid Mech. **398**, 299 (1999).
[26] J. Scoffoni, E. Lajeunesse, and G. M. Homsy, "Interface instabilities during displacement of two miscible fluids in a vertical pipe," Phys. Fluids **13**, 553 (2001).
[27] C. Gabard and J.-P. Hulin, "Miscible displacement of non-Newtonian fluids in a vertical tube," Eur. Phys. J. E **11**, 231 (2003).
[28] Q. Cao, L. Ventresca, K. R. Sreenivas, and A. K. Prasad, "Instability due to viscosity stratification downstream of a centreline injector," Can. J. Chem. Eng. **81**, 913 (2003).
[29] M. d'Olce, J. Martin, N. Rakotomalala, D. Salin, and L. Talon, "Pearl and mushroom instability patterns in two miscible fluids' core annular flows," Phys. Fluids **20**, 024104 (2008).
[30] Z. Yang and Y. C. Yortsos, "Asymptotic solutions of miscible displacements in geometries of large aspect ratio," Phys. Fluids **9**, 286 (1997).
[31] N. Goyal, H. Pichler, and E. Meiburg, "Variable-density miscible displacements in a vertical Hele-Shaw cell: Linear stability,"
J. Fluid Mech. **584**, 357 (2007).
[32] K. C. Sahu, H. Ding, P. Valluri, and O. K. Matar, "Pressure-driven miscible two-fluid channel flow with density gradients," Phys. Fluids **21**, 043603 (2009).
[33] S. M. Taghavi, T. Séon, D. M. Martinez, and I. A. Frigaard, "Influence of an imposed flow on the stability of a gravity current in a near horizontal duct," Phys. Fluids **22**, 031702 (2010).
[34] S. M. Taghavi, T. Séon, D. M. Martinez, and I. A. Frigaard, "Stationary residual layers in buoyant Newtonian displacement flows," Phys. Fluids **23**, 044105 (2011).
[35] S. M. Mohammadi, M. Carrasco-Teja, S. Storey, I. A. Frigaard, and D. M. Martinez, "An experimental study of laminar displacement flows in narrow vertical eccentric annuli," J. Fluid Mech. **649**, 371 (2010).
[36] A. K. Gunstensen, D. H. Rothman, S. Zaleski, and G. Zanetti, "Lattice Boltzmann model for immiscible fluids," Phys. Rev. A **43**, 4320 (1991).
[37] X. Shan and H. Chen, "Lattice Boltzmann model for simulating flows with multiple phases and components," Phys. Rev. E. **47**, 1815 (1993).
[38] X. Shan and G. Doolen, "Multicomponent lattice-Boltzmann model with interparticle interaction," J. Stat. Phys. **81**, 379 (1995).
[39] M. R. Swift, W. R. Osborn, and J. M. Yeomans, "Lattice-Boltzmann simulation of nonideal fluids," Phys. Rev. Lett. **75**, 830 (1995).
[40] X. He, R. Zhang, S. Chen, and G. D. Doolen, "On the three-dimensional Reyleigh-Taylor instability," Phys. Fluids **11**(5), 1143 (1999).
[41] S. Chen and G. D. Doolen, "Lattice Boltzmann method for fluid flows," Ann. Rev. Fluid Mech. **30**, 329 (1998).
[42] R. Zhang, X. He, and S. Chen, "Interface and surface tension in incompressible lattice Boltzmann multiphase model," Comput. Phys. Commun. **129**, 121 (2000).
[43] K. C. Sahu and S. P. Vanka, "A multiphase lattice Boltzmann study of buoyancy-induced mixing in a tilted channel," Comput. Fluids **50**, 199 (2011).
[44] N. Rakotomalala, D. Salin, and P. Watzky, "Miscible displacement between two parallel plates: BGK lattice gas simulations," J. Fluid Mech. **338**, 277 (1997).
[45] C. E. Hickox, "Instability due to viscosity and density stratification in axisymmetric pipe flow," Phys. Fluids **14**, 251 (1971).
[46] J. Chin, E. S. Boek, and P. V. Coveney, "Lattice Boltzmann simulation of the flow of binary immiscible fluids with different viscosities using the Shan-Chen microscopic interaction model," Philos. Trans. R. Soc. London, Ser. A **360**, 547 (2002).
[47] P. Grosfils, J. P. Boon, and J. Chin, "Structural and dynamical characterization of Hele-Shaw viscous fingering," Philos. Trans. R. Soc. London, Ser. A **362**, 1723 (2004).
[48] Q. Kang, D. Zhang, and S. Chen, "Immiscible displacement in a channel: Simulations of fingering in two dimensions," Adv. Water Resour. **27**, 13 (2004).
[49] B. Dong, Y. Y. Yan, W. Li, and Y. Song, "Lattice Boltzmann simulation of viscous fingering phenomenon of immiscible fluids displacement in a channel," Comput. Fluids **39**, 768 (2010).
[50] P. L. Bhatnagar, E. P. Gross, and M. Krook, "A model for collision process in gases. I. Small amplitude processes in charged and neutral one-component system," Phys. Rev. **94**, 511 (1954).
[51] N. F. Carnahan and K. E. Starling, "Equation of state for non-attracting rigid spheres," J. Chem. Phys. **51**, 635 (1969).
[52] K. N. Premnath and J. Abraham, "Lattice Boltzmann model for axisymmetric multiphase flows," Phys. Rev. E **71**, 056706 (2005).
[53] Q. Chang and J. I. D. Alexander, "Application of the lattice Boltzmann method to two-phase Rayleigh-Benard convection with a deformable interface," J. Comput. Phys. **212**, 473 (2006).
[54] A. Fakhari and M. H. Rahimian, "Simulation of falling droplet by the lattice Boltzmann method," Commun. Nonlinear Sci. Numer. Simul. **14**, 3046 (2009).
[55] A. Fakhari and M. H. Rahimian, "Investigation of deformation and breakup of a moving droplet by the method of lattice Boltzmann equations," Int. J. Numer. Methods Fluids **64**, 827 (2010).
[56] T. Lee and C.-L. Lin, "A stable discretization of the lattice Boltzmann equation for simulation of incompressible two-phase

flows at high density ratio," J. Comput. Phys. **206**, 16 (2005).
[57] R. Evans, "The nature of the liquid-vapor interface and other topics in the statistical mechanics of non-uniform classical fluids," Adv. Phys. **28**, 143 (1979).
[58] P. R. Redapangu, S. P. Vanka, and K. C. Sahu, "Multiphase lattice Boltzmann simulations of buoyancy-induced flow of two immiscible fluids with different viscosities," Eur. J. Mech. B/Fluids **34**, 105 (2012).
[59] P. G. Saffman and G. I. Taylor, "The penetration of a fluid into a porous medium or Hele-Shaw cell containing a more viscous liquid," Proc. R. Soc. London, Ser. A **245**, 312 (1958).
[60] S. M. Taghavi, T. Séon, D. M. Martinez, and I. A. Frigaard, "Buoyancy-dominated displacement flows in near-horizontal channels: The viscous limit," J. Fluid Mech. **639**, 1 (2009).
[61] S. M. Taghavi, K. Alba, T. Séon, K. Wielage-Burchard, D. M. Martinez, and I. A. Frigaard, "Miscible displacement flows in near-horizontal ducts at low Atwood number," J. Fluid Mech. **696**, 175 (2012).
[62] T. Séon, D. Salin, J. P. Hulin, B. Perrin, and E. J. Hinch, "Buoyancy driven front dynamics in tilted tubes," Phys. Fluids **17**, 031702 (2005).
[63] K. C. Sahu and O. K. Matar, "Three-dimensional convective and absolute instabilities in pressure-driven two-layer channel flow," Int. J. Numer. Methods Fluids **37**, 987 (2011).